

Graphical Abstract

LoLA-SpecViT: Local Attention SwiGLU Vision Transformer with LoRA for Hyperspectral Imaging

Fadi Abdeladhim Zidi, Djamel Eddine Boukhari, Abdellah Zakaria Sellam, Abdelkrim Ouafi, Cosimo Distanto, Salah Eddine Bekhouche, Abdelmalik Taleb-Ahmed

Highlights

LoLA-SpecViT: Local Attention SwiGLU Vision Transformer with LoRA for Hyperspectral Imaging

Fadi Abdeladhim Zidi, Djamel Eddine Boukhari, Abdellah Zakaria Sellam, Abdelkrim Ouafi, Cosimo Distanto, Salah Eddine Bekhouche, Abdelmalik Taleb-Ahmed

- LoLA-SpecViT: hierarchical spectral Vision Transformer with local windowed attention
- LoRA fine-tuning reduces trainable parameters by over 80% for efficiency
- SwiGLU activations and cyclical LoRA scheduler boost convergence and generalisation
- Achieves up to 99.91% overall accuracy on WHU-LongKou, HongHu and Salinas datasets

LoLA-SpecViT: Local Attention SwiGLU Vision Transformer with LoRA for Hyperspectral Imaging

Fadi Abdeladhim Zidi

VSC Laboratory, Department of Electrical Engineering, University of Mohamed Khider, Biskra, 07000, Biskra, Algeria

Djamel Eddine Boukhari

Scientific and Technical Research Centre for Arid Areas (CRSTRA), Biskra, 07000, Biskra, Algeria

Abdellah Zakaria Sellam

Department of Innovation Engineering, University of Salento & Institute of Applied Sciences and Intelligent Systems – CNR, Via per Monteroni, Lecce, 73100, Lecce, Italy

Abdelkrim Ouafi

VSC Laboratory, Department of Electrical Engineering, University of Mohamed Khider, Biskra, 07000, Biskra, Algeria

Cosimo Distante

Institute of Applied Sciences and Intelligent Systems – CNR, Via per Monteroni, Lecce, 73100, Lecce, Italy

Salah Eddine Bekhouche

UPV/EHU, University of the Basque Country, Sebastian, 20018, Sebastian, Spain

Abdelmalik Taleb-Ahmed

Université Polytechnique Hauts-de-France, Université de Lille, CNRS, , Valenciennes, 59313, Hauts-de-France, France

Abstract

Hyperspectral image classification remains a challenging task due to the high dimensionality of spectral data, significant inter-band redundancy, and the limited availability of annotated samples. While recent transformer-based models have improved the global modeling of spectral-spatial dependencies, their scalability and adaptability under label-scarce conditions remain lim-

ited. In this work, we propose **LoLA-SpecViT**(Low-rank adaptation Local Attention Spectral Vision Transformer), a lightweight spectral vision transformer that addresses these limitations through a parameter-efficient architecture tailored to the unique characteristics of hyperspectral imagery. Our model combines a 3D convolutional spectral front-end with local window-based self-attention, enhancing both spectral feature extraction and spatial consistency while reducing computational complexity. To further improve adaptability, we integrate low-rank adaptation (LoRA) into attention and projection layers, enabling fine-tuning with over 80% fewer trainable parameters. A novel cyclical learning rate scheduler modulates LoRA adaptation strength during training, improving convergence and generalisation. Extensive experiments on three benchmark datasets WHU-Hi LongKou, WHU-Hi HongHu, and Salinas demonstrate that LoLA-SpecViT consistently outperforms state-of-the-art baselines, achieving up to 99.91% accuracy with substantially fewer parameters and enhanced robustness under low-label regimes. The proposed framework provides a scalable and generalizable solution for real-world HSI applications in agriculture, environmental monitoring, and remote sensing analytics. Our code is available in the following GitHub Repository.

Keywords: Hyperspectral image classification, Vision Transformer, Parameter-efficient fine-tuning, Low-rank adaptation, Spectral attention, Local self-attention.

1. Introduction

Hyperspectral imaging (HSI) has fundamentally transformed observational remote sensing through its capacity to capture hundreds of contiguous, narrow spectral bands at each ground location, generating comprehensive three-dimensional data cubes that substantially exceed the limited information provided by RGB or multispectral sensors Zhang et al. (2021); Huang et al. (2024). This enhanced spectral resolution has revolutionized agricultural monitoring capabilities by delivering unprecedented precision in crop analysis (Zhou et al., 2023a). Within agricultural contexts, these spectral signatures reveal subtle biochemical and structural characteristics that include early stress indicators, nutrient deficiencies, and moisture variations, all of which remain undetectable to conventional imaging systems. For instance, hyperspectral data enables early detection of drought stress or pathogen in-

fection before visible symptoms appear, facilitates precise discrimination between crops and weeds for targeted herbicide application, and supports accurate estimation of chlorophyll levels and crop maturity for optimal harvest timing García-Vera et al. (2024); Fadi and Abdelkrim (2024); Wang et al. (2024); Zidi et al. (2025). These capabilities highlight why precision agriculture has emerged as a key application domain for HSI technology Ram et al. (2024). However, these significant opportunities are accompanied by substantial technical challenges that hinder HSI’s practical implementation. The curse of dimensionality frequently overwhelms classical classification algorithms, while spectral variability from illumination and atmospheric conditions can severely compromise material identification accuracy. Furthermore, the fundamental trade-off between spectral richness and spatial resolution often limits effective real-world deployment Plaza and Benediktsson (2019); Chen et al. (2020); Li et al. (2022). These concurrent opportunities and obstacles necessitate the development of innovative deep-learning frameworks capable of efficiently distilling high-dimensional spectra into robust, discriminative features while preserving critical spatial-spectral relationships Ma and Zhang (2023).

Early deep-learning methods for HSI classification focused primarily on convolutional architectures. Li et al. (2017a) introduced a 3D-CNN to jointly learn local spectral-spatial features, demonstrating strong performance on datasets with limited labeled samples. Subsequent studies confirmed that while CNNs effectively extract hierarchical features, they require millions of parameters and extensive data augmentation to capture long-range dependencies Liu and Zhang (2025). In response, transformer-based architectures have emerged as a compelling alternative. By tokenising hyper-spectral cubes and applying self-attention, Vision Transformers (ViTs) can model global spectral-spatial dependencies without relying on deep convolutional stacks (He and Zhou, 2024; Chen and Huang, 2024). However, the quadratic complexity of standard self-attention concerning sequence length makes vanilla ViTs computationally prohibitive for large-scale HSI volumes. To reconcile locality and global context, recent hybrid CNN–Transformer architectures interleave multi-scale convolutions with windowed self-attention. For instance, Cai et al. (2022) proposed a coarse-to-fine sparse attention mechanism, while Hu et al. (2024) introduced selective spectral attention windows to prune redundant computations. Despite these advances, hybrid designs often underutilise inter-band correlations or retain large parameter footprints—challenges directly addressed by our proposed

LoLA-SpecViT architecture.

To systematically address these identified bottlenecks while leveraging the proven strengths of transformer architectures, we introduce LoLA-SpecViT, a hierarchical vision transformer architecture that strategically combines a lightweight 3D convolutional spectral front-end with windowed self-attention blocks utilizing SwiGLU activations. Our approach addresses the computational limitations of standard transformers while preserving their global modeling capabilities. We further enhance both efficiency and generalisation through the implementation of a novel BandDropout mechanism for spectral regularisation and a specialised spectral attention module that explicitly models inter-band correlations. Crucially, we employ Parameter-Efficient Fine-Tuning (PEFT) through a cyclic LoRA rate schedule (Hu et al., 2021; Lester et al., 2021), achieving a reduction in trainable parameters exceeding 80% while preserving global contextual information and attaining state-of-the-art classification accuracy across benchmark HSI datasets. This design represents a strategic integration of transformer efficiency improvements with domain-specific innovations for agricultural hyperspectral imaging applications. The main contributions of this work are summarised as follows.

- We propose LoLA-SpecViT, a novel hierarchical vision transformer architecture that combines windowed attention mechanisms with SwiGLU activations to model multi-scale spectral-spatial dependencies in hyperspectral data effectively.
- A spectral processing front-end based on 3D convolutions is designed with a novel BandDropout technique and spectral attention module to enhance band-wise feature learning while reducing overfitting risks.
- We incorporate parameter-efficient fine-tuning (PEFT) techniques, including a newly introduced Cyclic LoRA Rate (CLR) scheduling strategy, which improves training efficiency and significantly reduces computational costs.
- Extensive experiments on multiple benchmark hyperspectral datasets demonstrate that LoLA-SpecViT achieves state-of-the-art classification accuracy with lower resource requirements, confirming its effectiveness and superiority over existing methods.

The remainder of this paper is structured as follows: Section 2 surveys the relevant literature; Section 3 details the LoLA-SpecViT architecture; Sec-

tion 4 describes the experimental setup; Section 5 presents and analyses the findings; and Section 6 concludes the study with suggestions for future research.

2. Related Work

The field of HSI classification has progressed significantly over the past decade, shifting from conventional machine learning algorithms toward deep learning-based architectures designed to address the challenges of high-dimensional spectral-spatial analysis. This transition is shaped by the imperative to balance model expressiveness with scalability, particularly for applications requiring accurate, real-time interpretation of large-scale HSI data.

2.1. Deep Learning Foundations for HSI Classification

The transition from handcrafted to learned features has been transformative in HSI classification, enabling models to directly capture both spectral and spatial regularities from the data (Chen et al., 2021). Hu et al. (Hu et al., 2015) initiated this shift with pixel-wise multilayer perceptrons (MLPs), demonstrating baseline spectral discrimination but neglecting contextual information. Li et al. (Li et al., 2017b) subsequently introduced 2D convolutional neural networks (CNNs) for localized spatial filtering and later extended to 3D CNNs for unified spectral-spatial fusion, though at a significant computational expense. HybridSN (Roy et al., 2020) elegantly balances this trade-off by cascading 3D and 2D convolutions, yielding rich joint representations with controlled model complexity. To further enhance feature adaptability, Yang et al. (Yang et al., 2021) proposed A²MFE, which automatically adjusts receptive fields via multi-scale convolutions, and Sun et al. (Sun et al., 2022) developed SSFTT, a spectral-spatial feature tokenization transformer that first extracts low-level features through 3D-2D CNNs before feeding Gaussian-weighted tokens into a Transformer encoder. Attention-driven designs such as MADANet Cui et al. (2023), which integrates multiscale feature aggregation with dual attention, and HiT (Yang et al., 2022), which embeds spectral-adaptive 3D convolutions within a pure Transformer pipeline, have delivered further gains. Complementing these, LANet (Ding et al., 2021) embeds local attention modules into a shallow encoder-decoder, enriching low-level semantic features for improved segmentation and classification performance. As these architectures deepen, their resource demands escalate, challenging deployment on edge and embedded

platforms. Lei et al. (Lei et al., 2023) address redundancy via collaborative pruning, while Yue et al. (Yue et al., 2022) and Yu et al. (Yu et al., 2024) demonstrate that self-supervised and prototype-based distillation preserve accuracy under severe compression. More recently, Ma et al. (Ma et al., 2024) and Zhang et al. (Zhang et al., 2024a) introduced AS2MLP and LDS2MLP, respectively adaptive MLP variants that fuse convolutional priors with learnable spatial shifts, offering near-global receptive fields with minimal overhead. Despite these advances, purely convolutional and shallow MLP frameworks remain challenged by the need to model long-range spectral dependencies across hundreds of contiguous bands, motivating the exploration of transformer-based and hybrid paradigms.

2.2. *Vision Transformers and Hybrid Architectures for Global Modeling*

Vision Transformers (ViTs) reformulate images as sequences of tokens and apply self-attention to capture global dependencies, dispensing with convolutional locality constraints. Dosovitskiy et al. (Dosovitskiy et al., 2021) first demonstrated this on RGB imagery; Ibáñez et al. (Ibanez et al., 2022) then introduced HSIMAE, a masked autoencoder that pretrains robust spectral embeddings under label scarcity. Cross SSL (Bai et al., 2024) extends self-supervision to learn representations transferable across sensors and environments. Sun et al. (Sun et al., 2024) further mitigate spectral redundancy with MASSFormer’s memory-augmented self-attention and spatial-spectral positional encoding. To control Transformer complexity, Zhou et al. (Zhou et al., 2023b) proposed DiCT, dynamically pruning low-importance tokens. Hybrid designs fuse local inductive biases with global attention. Arshad et al. (Arshad and Ullah, 2024) present Hybrid-ViT, pairing a residual 3D CNN with a transformer and channel-attention module to capture complementary cues. Zhang et al. (Zhang et al., 2023)’s 3D-CmT fuses 3D-CNN frontends with a transformer encoder for multiscale spectral-spatial modeling. Xu et al. (Xu et al., 2024)’s DBCTNet employs dual branches one 3D CNN, and one Transformer for balanced context integration, while Ma et al. (Ma and Others, 2023)’s LSGA introduces light self-Gaussian attention for efficient feature discrimination. Recognizing the need for hierarchical abstraction, Ahmad et al. (Ahmad et al., 2024) proposed the Hir-Transformer (Pyramid Hierarchical Transformer), which organises tokens across multiple levels to capture both local detail and global structure effectively. State-space transformer variants now offer linear scalability. SSMamba and MorpMamba

(Ahmad et al., 2025) integrate structured state-space modules with morphological operations, achieving long-sequence modelling at linear cost. Finally, E-SR-SSIM (Hu et al., 2023) employs subspace partitioning guided by structural similarity to select representative bands, reducing redundancy while enhancing interpretability. While these approaches successfully address the locality limitations of CNNs, they introduce their own computational challenges. The quadratic complexity of self-attention mechanisms concerning sequence length creates scalability issues when processing large HSI volumes, necessitating further innovations in efficient attention computation and model compression strategies.

2.3. Efficiency-Oriented Architectures and Optimization Strategies

Recognising the computational and memory constraints imposed by both deep CNNs and standard transformers, recent research has focused on developing lightweight architectures and optimisation strategies that maintain classification performance while reducing computational overhead. Khan et al. (Khan et al., 2024) introduced GroupFormer, which partitions spectral bands into discrete groups and performs intra-group self-attention, effectively reducing computational complexity from quadratic to linear concerning the number of spectral bands without sacrificing classification accuracy. Advancing this efficiency-focused paradigm, Zhu et al. (Zhu et al., 2023) developed PatchOut, which replaces fixed-size spatial patching with learned token sampling mechanisms to streamline the encoding process. While this approach significantly reduces computational requirements, it potentially risks losing fine-grained spatial details crucial for accurate classification. Fu et al. (Fu et al., 2025) incorporated Convolutional Block Attention Module (CBAM) based adaptive pruning to dynamically eliminate redundant channels and spatial locations during inference, providing runtime efficiency improvements. These efficiency-oriented strategies achieve substantial reductions in parameter counts and inference times but often overlook cross-group dependencies in grouped approaches or require dataset-specific threshold tuning for pruning mechanisms. Furthermore, these methods typically focus on architectural modifications rather than addressing the fundamental challenge of adapting large-scale pre-trained models to the specific characteristics of hyperspectral data.

2.4. *Efficient Adaptation of Large Pre-trained Models*

The limitations identified in existing approaches highlight a critical gap in HSI classification research: the need for methods that can leverage the representational power of large pre-trained models while maintaining computational efficiency and adapting effectively to the unique characteristics of hyperspectral data. PEFT addresses this challenge by adapting large pre-trained models to downstream tasks through updating only a small fraction of parameters ($|\Delta\theta| \ll |\theta|$), thereby substantially reducing both computational and storage overheads (Xin et al., 2024). PEFT approaches encompass several distinct methodologies. Adapter-based methods introduce lightweight trainable modules into each layer, exemplified by adapter tuning (Houlsby et al., 2019) and visual prompt tuning (VPT) (Jia et al., 2022). Unified tuning approaches, such as NOAH, combine multiple adapter variants within a single framework to jointly optimize diverse modules for improved flexibility and performance (Zhang et al., 2024b). Partial-parameter update strategies restrict fine-tuning to selected parameter subsets, including Bias-Only tuning (BitFit) (Ben Zaken et al., 2022), low-rank adaptation via LoRA (Hu et al., 2022), its Kronecker-product extension KronA (Edalati et al., 2022), and the hybrid Lokr method (Yeh et al., 2024). Recent enhancements in LoRA⁺ demonstrate that decoupling learning rates between low-rank factors can further increase fine-tuning efficiency (Hayou et al., 2024).

2.5. *Toward Generalizable and Efficient HSI Classification*

The comprehensive analysis of existing literature reveals several persistent challenges in HSI classification. Convolutional approaches, while computationally efficient, remain constrained by local receptive fields and struggle to capture long-range spectral dependencies. Standard transformer architectures successfully model global relationships but suffer from quadratic computational complexity. Efficiency-focused methods reduce computational overhead but often sacrifice either accuracy or cross-dependency modeling capabilities. Most critically, existing approaches fail to effectively leverage semantic knowledge from large-scale pre-trained models that could provide valuable contextual understanding for spectral-spatial feature interpretation.

3. Proposed Method

This section presents the proposed **LOLA-SpecViT** (Low-Rank Adapted Vision Transformer with Spectral Optimization), a novel parameter-efficient

architecture tailored for hyperspectral image classification. The architecture, illustrated in Figure 1, integrates spectral-spatial feature learning with parameter-efficient fine-tuning through Low-Rank Adaptation (LoRA). LOLA-SpecViT comprises four main components: (1) PCA-based dimensionality reduction, (2) spectral processing front-end, (3) hierarchical transformer backbone with LoRA integration, and (4) classification head with enhanced feature projection.

3.1. Input Preprocessing and PCA Dimensionality Reduction

Given a raw hyperspectral image $\mathbf{X}_{\text{raw}} \in \mathbb{R}^{H \times W \times C_{\text{raw}}}$ where $H \times W$ represents spatial dimensions and C_{raw} is the original number of spectral bands, we first apply Principal Component Analysis (PCA) for dimensionality reduction and spectral decorrelation. The input is reshaped to matrix form and centred:

$$\mathbf{X}_{\text{flat}} = \text{Reshape}(\mathbf{X}_{\text{raw}}) \in \mathbb{R}^{(H \times W) \times C_{\text{raw}}} \quad (1)$$

$$\mathbf{\Sigma} = \frac{1}{HW - 1} (\mathbf{X}_{\text{flat}} - \boldsymbol{\mu})^T (\mathbf{X}_{\text{flat}} - \boldsymbol{\mu}) \quad (2)$$

where $\boldsymbol{\mu}$ is the mean spectral vector. The PCA transformation with whitening is computed as follows:

$$\mathbf{\Sigma} = \mathbf{V} \mathbf{\Lambda} \mathbf{V}^T \quad (3)$$

$$\mathbf{X}_{\text{pca}} = (\mathbf{X}_{\text{flat}} - \boldsymbol{\mu}) \mathbf{V}_k \mathbf{\Lambda}_k^{-1/2} \quad (4)$$

where $\mathbf{V}_k \in \mathbb{R}^{C_{\text{raw}} \times k}$ contains the first k eigenvectors corresponding to the largest eigenvalues, and $\mathbf{\Lambda}_k$ contains the corresponding eigenvalues. The result is reshaped back to spatial format:

$$\mathbf{X}_{\text{in}} = \text{Reshape}(\mathbf{X}_{\text{pca}}) \in \mathbb{R}^{H \times W \times k} \quad (5)$$

3.1.1. Patch Extraction and Tensor Preparation

For network processing, spatial patches of size $p \times p$ are extracted and prepared for batch processing:

$$\mathbf{F}_{\text{in}} = \text{BatchPatch}(\mathbf{X}_{\text{in}}) \in \mathbb{R}^{B \times k \times p \times p} \quad (6)$$

where B is the batch size, k is the number of principal components, and p is the spatial patch size.

3.2. Spectral Processing Front-End

The spectral processing stage extracts hierarchical spectral-spatial features through a series of 3D convolutions. The input tensor is first reshaped to enable 3D convolution operations:

$$\tilde{F}_{\text{in}} = \text{Unsqueeze}(F_{\text{in}}) \in \mathbb{R}^{B \times 1 \times k \times p \times p} \quad (7)$$

The spectral feature extraction follows a progressive convolution pipeline:

$$F_1 = \text{Swish} \left(\text{BatchNorm3d} \left(\text{Conv3d}_{(7,3,3)}(\tilde{F}_{\text{in}}) \right) \right) \quad (8)$$

$$F_2 = \text{Swish} \left(\text{BatchNorm3d} \left(\text{Conv3d}_{(5,3,3)}(F_1) \right) \right) \quad (9)$$

$$F_{\text{spec}} = \text{Swish} \left(\text{BatchNorm3d} \left(\text{Conv3d}_{(3,3,3)}(F_2) \right) \right), \quad (10)$$

where $\text{Conv3d}_{(k_d, k_h, k_w)}$ denotes 3D convolution with kernel size (k_d, k_h, k_w) along the depth (spectral), height, and width dimensions, respectively. The resulting output tensor F_{spec} takes the form $\mathbb{R}^{B \times \text{dim} \times D \times H \times W}$, where D denotes the spectral dimension after the 3D convolutions, corresponding to the number of processed spectral features. The Swish activation function is defined as:

$$\text{Swish}(x) = x \cdot \sigma(x) = x \cdot \frac{1}{1 + e^{-x}} \quad (11)$$

This activation function promotes better gradient flow compared to ReLU and has been shown to improve convergence in deep networks.

3.2.1. Band Dropout Regularization

To enhance spectral robustness and prevent overfitting to specific spectral patterns, we introduce a **BandDropout** regularisation mechanism that randomly masks spectral channels during training:

$$M \sim \text{Bernoulli}(1 - p_{\text{drop}}) \quad (12)$$

$$F_{\text{bdrop}} = \frac{F_{\text{spec}} \odot M}{1 - p_{\text{drop}}} \quad (13)$$

where $M \in \{0, 1\}^{C_{\text{spec}}}$ is a binary mask sampled from a Bernoulli distribution with dropout probability p_{drop} , \odot denotes element-wise multiplication, and the normalization factor $(1 - p_{\text{drop}})^{-1}$ maintains the expected magnitude of activations.

3.2.2. Spectral Attention Mechanism

To adaptively emphasize the most discriminative spectral features, we employ a **SpectralAttention** module that learns channel-wise attention weights: **Global Spectral Pooling**:

$$\mathbf{z} = \text{GAP}(F_{\text{bdrop}}) \in \mathbb{R}^{B \times C_{\text{spec}}} \quad (14)$$

where GAP denotes Global Average Pooling over spatial dimensions:

$$z_c = \frac{1}{H_{\text{spec}} \cdot W_{\text{spec}} \cdot D_{\text{spec}}} \sum_{d=1}^{D_{\text{spec}}} \sum_{h=1}^{H_{\text{spec}}} \sum_{w=1}^{W_{\text{spec}}} F_{\text{bdrop}}(b, c, d, h, w) \quad (15)$$

The attention weights are computed through a two-layer MLP with bottleneck architecture:

$$A_{\text{spec}} = \sigma(\mathbf{W}_2 \cdot \text{Swish}(\mathbf{W}_1 \cdot \mathbf{z})) \quad (16)$$

where $\mathbf{W}_1 \in \mathbb{R}^{r \times C_{\text{spec}}}$ and $\mathbf{W}_2 \in \mathbb{R}^{C_{\text{spec}} \times r}$ are learned projection matrices, $r < C_{\text{spec}}$ is the bottleneck dimension (typically $r = C_{\text{spec}}/4$), and $\sigma(\cdot)$ is the sigmoid activation function. **Feature Recalibration**: The final spectrally attended features are obtained by:

$$F_{\text{attended}} = F_{\text{bdrop}} \odot \text{Reshape}(A_{\text{spec}}) \quad (17)$$

3.2.3. Spatial Dimension Reduction

To prepare features for the transformer backbone, we reduce the spectral dimension through averaging and apply spatial patch embedding:

$$F_{\text{spatial}} = \text{Mean}(F_{\text{attended}}, \text{dim} = 2) \in \mathbb{R}^{B \times C_{\text{spec}} \times H_{\text{spec}} \times W_{\text{spec}}} \quad (18)$$

$$F_{\text{embed}} = \text{Swish}(\text{BatchNorm2d}(\text{Conv2d}_{4 \times 4, \text{stride}=2}(F_{\text{spatial}}))) \quad (19)$$

3.3. Hierarchical Transformer Backbone with LoRA Integration

The LOLA-SpecViT processes the embedded features through a three-stage hierarchical transformer pipeline. Each stage i consists of a backbone module \mathcal{B}_i followed by a downsampling operation \mathcal{D}_i :

$$\mathbf{X}_i = \mathcal{D}_i(\mathcal{B}_i(\mathbf{X}_{i-1})) \quad (20)$$

where $\mathbf{X}_0 = F_{\text{embed}}$ is the input to the first stage. **Progressive Feature Scaling**: Each downsampling operation halves the spatial resolution while doubling the channel dimension:

$$\mathbf{X}_0 \in \mathbb{R}^{B \times H_0 \times W_0 \times C_0}, \quad \mathbf{X}_1 \in \mathbb{R}^{B \times H_0/2 \times W_0/2 \times 2C_0}, \quad (21)$$

$$\mathbf{X}_2 \in \mathbb{R}^{B \times H_0/4 \times W_0/4 \times 4C_0}, \quad \mathbf{X}_3 \in \mathbb{R}^{B \times H_0/8 \times W_0/8 \times 8C_0} \quad (22)$$

3.3.1. LoRA-Enhanced Window Attention

Each backbone module \mathcal{B}_i integrates Low-Rank Adaptation (LoRA) into the self-attention mechanism for parameter-efficient fine-tuning. Input features are partitioned into non-overlapping windows of size $M \times M$:

$$\mathbf{W}_j = \text{WindowPartition}(\mathbf{X}_{i-1}, M) \in \mathbb{R}^{B \cdot N_w \times M^2 \times C_i} \quad (23)$$

where $N_w = \frac{H_i \cdot W_i}{M^2}$ is the number of windows. For each window $\mathbf{x}_w \in \mathbb{R}^{M^2 \times C_i}$, queries, keys, and values are computed using LoRA-augmented linear transformations:

$$\begin{aligned} \mathbf{Q} &= \mathbf{x}_w \mathbf{W}_q + \alpha_q \cdot \mathbf{x}_w \mathbf{A}_q \mathbf{B}_q, & \mathbf{K} &= \mathbf{x}_w \mathbf{W}_k + \alpha_k \cdot \mathbf{x}_w \mathbf{A}_k \mathbf{B}_k, \\ \mathbf{V} &= \mathbf{x}_w \mathbf{W}_v + \alpha_v \cdot \mathbf{x}_w \mathbf{A}_v \mathbf{B}_v \end{aligned} \quad (24)$$

The matrices \mathbf{W}_q , \mathbf{W}_k , and \mathbf{W}_v are the frozen, pre-trained weight matrices of shape $\mathbb{R}^{C_i \times d_{\text{head}}}$. In contrast, \mathbf{A}_q , \mathbf{A}_k , and \mathbf{A}_v are trainable down-projection matrices in $\mathbb{R}^{C_i \times r}$, while \mathbf{B}_q , \mathbf{B}_k , and \mathbf{B}_v are trainable up-projection matrices in $\mathbb{R}^{r \times d_{\text{head}}}$. Here, the LoRA rank r is chosen such that $r \ll \min(C_i, d_{\text{head}})$, and the scaling factors α_q , α_k , and α_v are typically set to $\text{lora_alpha}/r$. The attention mechanism incorporates relative position bias for better spatial modeling:

$$\text{Attention}(\mathbf{Q}, \mathbf{K}, \mathbf{V}) = \text{Softmax} \left(\frac{\mathbf{Q}\mathbf{K}^T}{\sqrt{d_k}} + \mathbf{B}_{\text{rel}} \right) \mathbf{V} \quad (25)$$

where $\mathbf{B}_{\text{rel}} \in \mathbb{R}^{M^2 \times M^2}$ is the relative position bias matrix. The attention output is processed through a LoRA-enhanced projection:

$$\mathbf{O} = \text{Attention}(\mathbf{Q}, \mathbf{K}, \mathbf{V}) \mathbf{W}_o + \alpha_o \cdot \text{Attention}(\mathbf{Q}, \mathbf{K}, \mathbf{V}) \mathbf{A}_o \mathbf{B}_o \quad (26)$$

To stabilize training dynamics and improve gradient flow, we employ **recharge-based residual connections** with learnable scaling parameters:

$$\mathbf{Y}_{\text{attn}} = \gamma_{\text{attn}} \cdot \mathbf{X} + \beta_{\text{attn}} + \text{DropPath}(\mathbf{O}) \quad (27)$$

where γ_{attn} and β_{attn} are learnable scalars initialized to 1 and 0 respectively, and DropPath is stochastic depth regularization.

3.3.2. *SwiGLU Feed-Forward Network*

Each transformer block includes a SwiGLU-based feed-forward network for enhanced non-linearity:

$$\text{SwiGLU}(\mathbf{x}) = (\text{Swish}(\mathbf{x}\mathbf{W}_1) \odot (\mathbf{x}\mathbf{W}_2))\mathbf{W}_3 \quad (28)$$

where $\mathbf{W}_1, \mathbf{W}_2 \in \mathbb{R}^{C_i \times d_{\text{ffn}}}$ and $\mathbf{W}_3 \in \mathbb{R}^{d_{\text{ffn}} \times C_i}$. The complete transformer block output is:

$$\mathbf{Y}_{\text{ffn}} = \gamma_{\text{ffn}} \cdot \mathbf{Y}_{\text{attn}} + \beta_{\text{ffn}} + \text{DropPath}(\text{SwiGLU}(\text{LayerNorm}(\mathbf{Y}_{\text{attn}}))) \quad (29)$$

3.3.3. *Downsampling Module*

The downsampling module reduces spatial complexity while preserving semantic information through a sophisticated compression pipeline: **Depth-wise Convolution and Residual Connection:**

$$\mathbf{X}' = \text{Swish}(\text{Conv2d}_{3 \times 3, \text{groups}=C_i}(\mathbf{X})), \quad \mathbf{X}'' = \mathbf{X} + \mathbf{X}'. \quad (30)$$

Squeeze-and-Excitation Attention:

$$\mathbf{z} = \text{GAP}(\mathbf{X}'') \in \mathbb{R}^{B \times C_i}, \quad \mathbf{s} = \sigma(\mathbf{W}_{\text{se2}} \text{Swish}(\mathbf{W}_{\text{se1}} \mathbf{z})), \quad \mathbf{X}''' = \mathbf{s} \odot \mathbf{X}''. \quad (31)$$

Pointwise Convolution and Spatial Reduction:

$$\mathbf{Y} = \text{BatchNorm2d}(\text{Conv2d}_{1 \times 1}(\mathbf{X}''')), \quad \mathbf{Z} = \text{Conv2d}_{3 \times 3, \text{stride}=2}(\mathbf{Y}). \quad (32)$$

3.4. *Classification Head and Output Processing*

3.4.1. *Global Feature Aggregation*

The final backbone block produces spatial features that are globally aggregated for classification:

$$\mathbf{f}_{\text{global}} = \text{GAP}(\text{LayerNorm}(\mathcal{B}_3(\mathbf{X}_2))) \in \mathbb{R}^{B \times C_{\text{final}}} \quad (33)$$

3.4.2. *LoRA-Enhanced Classification Head*

The classification is performed using a LoRA-enhanced linear layer:

$$\hat{\mathbf{y}} = \mathbf{f}_{\text{global}} \mathbf{W}_{\text{cls}} + \alpha_{\text{cls}} \cdot \mathbf{f}_{\text{global}} \mathbf{A}_{\text{cls}} \mathbf{B}_{\text{cls}} \quad (34)$$

where $\mathbf{W}_{\text{cls}} \in \mathbb{R}^{C_{\text{final}} \times N_{\text{classes}}}$ is the frozen classification weight matrix, and $\mathbf{A}_{\text{cls}} \in \mathbb{R}^{C_{\text{final}} \times r_{\text{cls}}}$, $\mathbf{B}_{\text{cls}} \in \mathbb{R}^{r_{\text{cls}} \times N_{\text{classes}}}$ are the trainable LoRA adaptation matrices.

3.4.3. *Probability Distribution and Prediction*

The final class probabilities are obtained through softmax normalization:

$$P(c|\mathbf{x}) = \frac{\exp(\hat{y}_c)}{\sum_{j=1}^{N_{\text{classes}}} \exp(\hat{y}_j)} \quad (35)$$

The predicted class is determined by:

$$\hat{c} = \arg \max_{c \in \{1, \dots, N_{\text{classes}}\}} P(c|\mathbf{x}) \quad (36)$$

LOLA-SpecViT is a lightweight yet expressive architecture for hyperspectral image classification that markedly reduces trainable parameters via Low-Rank Adaptation (LoRA) while preserving full model capacity. It fuses 3D spectral convolutions with a hierarchical 2D transformer backbone, capturing both fine spectral signatures and broader spatial patterns. A window-based attention scheme—with relative position bias and LoRA-enhanced projections—cuts attention complexity from quadratic to linear, and additional techniques like spectral attention, band-dropout regularization, and cyclical LoRA scaling bolster robustness and training stability. Its modular design adapts easily to varied spectral resolutions and spatial scales, offering a practical, high-performance solution for real-world remote-sensing tasks.

4. Experiments

4.1. *Dataset*

In this work, we employ three publicly available hyperspectral datasets WHU-Hi-LongKou, WHU-Hi-HongHu, and Salinas to evaluate our classification framework under diverse agricultural scenarios comprehensively. These datasets differ in spatial resolution, spectral coverage, scene complexity, and number of land-cover classes, providing a robust basis for assessing model generalizability. **WHU-Hi-LongKou** dataset was acquired on 17 July 2018 in Longkou Town using a Headwall Nano-Hyperspec sensor mounted on a DJI Matrice 600 Pro UAV. The imagery covers a 550×400 -pixel area at approximately 0.463m spatial resolution and spans 270 spectral bands ranging from 400 nm to 1000 nm. It depicts a simple agricultural scene containing six main crops: corn, cotton, sesame, broadleaf soybean, narrowleaf soybean, and rice. The provided ground truth defines nine land-cover classes, including the six crops plus water, built-up area, and mixed weeds RSIDEA group,

Wuhan University (2018). **WHU-Hi-HongHu** dataset was collected on 20 November 2017 in Honghu City using the same Nano-Hyperspec sensor on a DJI Matrice 600 Pro UAV. This image is 940×475 pixels in size, with 270 spectral bands at 0.043 m spatial resolution. The scene represents a complex agricultural testbed with numerous crop types alongside non-crop features such as roads, rooftops, and bare soil. The ground truth comprises 22 land-cover classes across vegetation and infrastructure categories RSDIEA group, Wuhan University (2017). **Salinas** scene is an airborne hyperspectral image of agricultural land in Salinas Valley, California, USA. It was acquired by NASA’s AVIRIS instrument at 3.7 m ground sampling distance. The scene is 512×217 pixels, with 224 original bands. Describe vegetable fields, vineyards, and bare soils, and is annotated in 16 classes of land cover CCWintco (Elhami et al.) (2004).

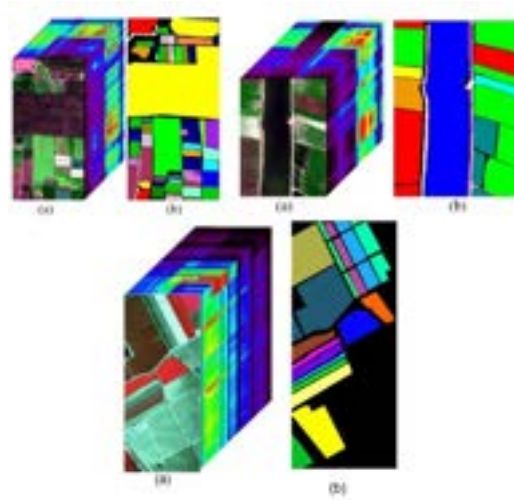


Figure 2: Visualization of hyperspectral data cubes and corresponding ground-truth classification maps for the WHU-Hi-HongH, WHU-Hi-Longkou, and Salinas datasets: (a) hyperspectral image cube; (b) ground-truth map.

4.2. Configurations

To ensure reproducibility and fair comparison, all experiments were conducted under a consistent hardware and software environment. The implementation was developed using the PyTorch framework and executed on a workstation equipped with an NVIDIA GeForce RTX 3080 GPU and 64 GB

of system RAM. We adopted the Adam optimizer with an initial learning rate of 1×10^{-3} . Models were trained for 100 epochs with a mini-batch size of 64. Each training instance consisted of hyperspectral patches of size $15 \times 15 \times 15$ (spectral \times height \times width), selected based on non-overlapping spatial windows. Our proposed LoLA-SpecViT was configured with three hierarchical stages, with depths of [3, 4, 19], embedding dimension of 96, and head counts of attention of [4, 8, 16]. Each stage employed a windowed self-attention mechanism with a fixed size of 7×7 . For regularization, we applied a drop path rate of 0.2 and integrated LoRA into attention layers using a rank of $r = 16$ and scaling factor $\alpha = 32$. To improve fine-tuning stability and efficiency, we employed a CLR scheduler designed for LoRA modules. The CLR policy oscillated the internal scaling factor between 0.8 and 1.5 using a ‘triangular2’ schedule with a step size of 100 iterations. This dynamic adjustment encouraged smoother convergence and better generalization across datasets.

5. Results

To validate our approach against the fundamental challenges of hyperspectral classification high-dimensional data, limited labels, and complex spectral variability we conduct a series of experiments on three benchmark datasets with only 2%, 5%, and 10% of samples for training. To evaluate the effectiveness of our hierarchical spectral transformer, we compare it against state-of-the-art methods, on the Longkou dataset. First, we compare global performance metrics against these baselines; then, we analyze class-specific results to illustrate how our model overcomes redundancy, captures subtle spectral differences, and mitigates overfitting under severe label scarcity.

5.1. Quantitative Performance Analysis

The evaluation of the WHU-Hi-HongHu dataset demonstrates that our proposed framework achieves state-of-the-art performance, attaining an OA of **99.55%**, an AA of **98.85%**, and a Kappa coefficient of **99.43%**. These results outperform the best existing method, DBCT, by 0.41%, 0.78%, and 0.52%, respectively, as shown in Table 1. These gains are particularly notable considering the experiments were conducted using only 10% of the available labeled data. The robustness of our approach under such a constrained supervision regime highlights the effectiveness of our spectral-processing front-end, which leverages BandDropout and channel-attention modules to emphasize

discriminative bands and suppress noise. Furthermore, the integration of LoRA for parameter-efficient adaptation and SwiGLU activations for improved non-linearity contribute to a more expressive and stable learning process, enabling the model to capture long-range spectral-spatial dependencies without overfitting.

Class-level comparisons further substantiate these improvements. The Cotton category achieves 99.93%, surpassing DBCT by 0.24%, which illustrates the model’s ability to capture intra-class spectral variations caused by factors such as crop density and soil background. The Rape class, which is frequently misclassified due to spectral similarities with other Brassica species, sees an improvement of 0.36%, reaching 99.83%. Similarly, Film Covered Lettuce, a spectrally complex class affected by reflectance distortions due to plastic mulch, achieves 99.79%, outperforming LSGA by 0.63%. These results, along with consistent performance across both vegetative and non-vegetative classes, confirm the proposed model’s superior ability to model fine-grained spectral-spatial patterns and its generalization to heterogeneous and ambiguous regions in real-world HSI scenes.

Table 1: Overall, average, kappa and per-class accuracies (%) on the HongHu dataset (10% training samples) for Ours, HSIMAE Ibanez et al. (2022), HybridSN Roy et al. (2020), ViT Dosovitskiy et al. (2021), MASSFormer Sun et al. (2024), DBCT Xu et al. (2024) and LSGA Ma and Others (2023).

	Ours	HSIMAE	HybridSN	ViT	MASSFormer	DBCT	LSGA
Overall Accuracy (%)	99.55	96.24	96.76	96.76	98.14	<u>99.14</u>	99.02
Average Accuracy (%)	98.85	92.99	92.50	92.50	96.25	<u>98.07</u>	97.54
Kappa Score (%)	99.43	96.18	96.77	96.77	97.65	<u>98.91</u>	98.75
Red roof	99.59	97.40	98.46	97.84	98.99	98.27	<u>99.54</u>
Road	96.71	88.87	75.45	87.22	<u>97.25</u>	97.44	96.82
Bare soil	99.42	95.84	95.61	94.98	98.87	<u>99.01</u>	98.23
Cotton	99.93	98.13	99.40	98.48	99.31	<u>99.69</u>	99.65
Cotton firewood	<u>98.96</u>	78.73	88.93	84.61	94.76	98.32	99.14
Rape	99.83	98.81	98.41	98.60	99.11	<u>99.47</u>	99.34
Chinese cabbage	99.07	94.10	95.77	92.50	97.15	<u>98.81</u>	98.01
Pakchoi	97.34	87.53	93.72	87.50	94.16	<u>98.38</u>	96.59
Cabbage	99.33	98.14	97.91	97.91	<u>99.77</u>	99.71	99.82
Tuber mustard	<u>99.45</u>	94.97	93.73	92.90	98.03	98.53	99.94
Brassica parachinensis	99.12	91.95	91.88	88.10	95.53	<u>98.77</u>	97.75
Brassica chinensis	99.39	92.80	92.17	91.23	98.15	<u>98.42</u>	96.98
Small Brassica chinensis	99.16	92.68	94.22	91.70	94.73	<u>98.48</u>	97.63
Lactuca sativa	99.49	95.31	92.83	91.74	98.48	<u>99.02</u>	98.90
Celtuce	96.23	94.56	87.59	94.02	98.51	<u>98.18</u>	97.96
Film covered lettuce	99.79	98.14	97.30	97.69	97.03	98.59	<u>99.16</u>
Romaine lettuce	98.93	96.94	92.21	95.59	98.86	99.47	<u>99.32</u>
Carrot	98.96	90.37	89.72	93.51	95.90	95.16	<u>96.56</u>
White radish	<u>98.94</u>	95.63	91.73	91.34	95.61	90.11	99.51
Garlic sprout	98.06	88.67	89.22	86.62	93.85	<u>99.00</u>	97.48
Broad bean	98.16	85.15	83.35	84.24	87.52	<u>90.77</u>	91.62
Tree	98.76	91.16	95.38	88.90	88.02	<u>96.76</u>	98.08

Building upon these results, we further assess the generalizability of our framework on the Salinas dataset, which presents distinct spectral and spatial characteristics under semi-arid agricultural conditions. As shown in Table 2,

our model achieves an OA of **99.51%**, surpassing the previous state-of-the-art MADANet by 0.34 percentage points. The Average Accuracy also reaches **99.47%**, exceeding MADANet’s 99.12% by 0.35%, while the Kappa score rises to **99.46%**, improving upon SSFTT’s 98.46% by a full percentage point. These consistent gains, achieved with only 10% of labeled samples, reaffirm the robustness of our design. The adaptive BandDropout mechanism, in conjunction with spectral attention and LoRA-enhanced transformer blocks, contributes to more effective modeling of discriminative spectral-spatial patterns, while SwiGLU activations facilitate better noise filtering and convergence stability during training. At the class level, our framework demonstrates clear advantages in distinguishing spectrally overlapping or phenologically variable crop types. For example, the class *Grapes_untrained* attains a precision of **99.63%**, outperforming A2MFE by 1.81 percentage points, confirming the model’s ability to resolve background interference from soil and weeds. In *Lettuce_romaine_7wk*, which involves subtle variations in canopy maturity and shadowing, our method achieves perfect classification (**100.00%**), exceeding HiT by 0.58 percentage points. Additionally, the class *Corn_senesced_green_weeds*, known for its spectral ambiguity due to aging vegetation, is classified with **99.90%** accuracy, outperforming SSFTT’s 99.81%. These improvements, especially in the most challenging categories, underscore the model’s capacity to maintain fine-grained class discrimination across varied agricultural landscapes. These results on the Salinas dataset confirm that our method consistently excels across datasets with varying spectral complexity, fine-grained class structure, and geographic diversity. To further assess generalizability, we extend our evaluation to the WHU-Hi-LongKou dataset—a scenario characterized by simpler crop types and relatively homogeneous spectral distributions. The complete comparison is presented in Table 3, where our proposed framework again achieves the highest performance across all reported metrics. Specifically, it attains an OA of **99.91%**, outperforming the strongest competing model, Cross, by **0.13%**. Hybrid-ViT and Hir-Transformer, both relying on transformer-based architectures, follow with OA scores of **99.75%** and **99.68%**, respectively, falling short by at least **0.16%**. Our model also achieves the highest Average Accuracy (AA) of **99.71%**, providing a decisive improvement over Cross (**99.45%**), Hybrid-ViT (**99.36%**), and Hir-Transformer (**99.14%**). These gains reflect the advantages of our LoRA-enhanced hierarchical transformer backbone, which captures complex spectral-spatial dependencies while maintaining parameter efficiency. Spatial-spectral baselines such as SSMamba

Table 2: Overall, average, kappa and per-class precision (%) on the Salinas dataset (10% training samples) for Ours, MADANet Cui et al. (2023), A²MFE Yang et al. (2021), HybridSN Roy et al. (2020), SSFTT Sun et al. (2022), HiT Yang et al. (2022), and LANet Ding et al. (2021).

	Ours	MADANet	A ² MFE	HybridSN	SSFTT	HiT	LANet
Overall Accuracy (%)	99.51	<u>99.17</u>	98.56	97.05	98.61	97.83	96.67
Average Accuracy (%)	99.47	<u>99.12</u>	98.72	97.52	98.97	98.87	97.12
Kappa Score (%)	99.46	98.34	97.35	96.72	<u>98.46</u>	97.58	96.39
Brocoli_green_weeds_1	<u>99.83</u>	99.64	99.46	99.30	99.34	100.00	98.32
Brocoli_green_weeds_2	99.94	98.95	97.28	<u>99.96</u>	100.00	99.75	98.64
Fallow	98.82	98.90	97.99	98.16	<u>99.89</u>	100.00	95.09
Fallow_rough_plow	98.65	97.58	95.67	98.05	<u>99.34</u>	99.85	98.01
Fallow_smooth	98.92	<u>99.02</u>	98.85	98.42	99.50	97.59	98.73
Stubble	100.00	98.01	98.31	98.67	98.31	<u>99.92</u>	98.86
Celery	<u>99.97</u>	99.34	95.76	98.96	99.91	100.00	97.04
Grapes_untrained	99.63	97.77	<u>97.82</u>	92.70	97.80	95.81	96.49
Soil_vinyard_develop	<u>99.68</u>	98.23	97.56	98.53	100.00	100.00	93.11
Corn_senesced_green_weeds	99.90	95.91	95.23	95.44	<u>99.81</u>	98.19	94.27
Lettuce_romaine_4wk	98.54	98.86	97.45	98.08	<u>98.77</u>	99.42	97.19
Lettuce_romaine_5wk	99.71	99.23	98.34	99.33	99.89	<u>99.84</u>	98.42
Lettuce_romaine_6wk	<u>99.39</u>	100.00	99.21	99.02	97.02	100.00	98.58
Lettuce_romaine_7wk	100.00	99.34	98.12	98.21	98.96	<u>99.42</u>	98.07
Vinyard_untrained	98.78	<u>98.49</u>	94.55	92.29	95.52	92.53	92.46
Vinyard_vertical_trellis	99.75	98.36	93.23	80.43	99.49	<u>99.66</u>	90.11

and MorpMamba also yield strong results (OA: **99.51%** and **99.70%**; AA: **98.45%** and **99.25%**), yet remain outperformed by our framework. Furthermore, our model achieves the highest Kappa score of **99.89%**, ahead of Cross (**99.78%**), Hybrid-ViT (**99.68%**), and Hir-Transformer (**99.59%**). By contrast, the reconstruction-based E-SR-SSIM records substantially lower performance across all metrics, reinforcing the limitations of generative methods under low-label constraints. The per-class performance analysis presented

Table 3: Comparison of classification performance on the Longkou dataset with 10% training samples for Ours, Cross Bai et al. (2024), Hybrid-ViT Arshad and Ullah (2024), Hir-Transformer Ahmad et al. (2024), SSMamba Ahmad et al. (2025), MorpMamba Ahmad et al. (2025), and E-SR-SSIM Hu et al. (2023).

Metrics	Ours	Cross	Hybrid-ViT	Hir-Transformer	SSMamba	MorpMamba	E-SR-SSIM
Overall Accuracy (%)	99.91	<u>99.78</u>	99.75	99.68	99.51	99.70	94.43
Average Accuracy (%)	99.71	<u>99.45</u>	99.36	99.14	98.45	99.25	81.78
Kappa Score (%)	99.89	<u>99.78</u>	99.68	99.59	99.36	99.61	92.63

in Table 4 highlights our framework’s exceptional capacity to discriminate among all nine land-cover categories using only 10% of the available training samples. The model achieves an Overall Accuracy of 99.91%, supported by consistently near-perfect precision, recall, and F1-scores. These results underscore the effectiveness of our hierarchical spectral-transformer architecture under data-scarce conditions. Spectrally homogeneous classes such as *Rice*

Table 4: Per-class precision, recall, and F1-score for our method (10% training samples)

Class	Precision	Recall	F1-Score
Corn	0.9996	0.9999	0.9998
Cotton	0.9985	1.0000	0.9993
Sesame	1.0000	0.9941	0.9971
Broad-leaf soybean	0.9995	0.9996	0.9996
Narrow-leaf soybean	0.9960	0.9979	0.9969
Rice	0.9999	0.9999	0.9999
Water	0.9997	0.9997	0.9997
Roads and houses	0.9927	0.9914	0.9920
Mixed weed	0.9928	0.9921	0.9925
Overall Accuracy (Ours)			0.9991

and *Water* exemplify this robustness, each attaining precision, recall, and F1-scores of 99.99% and 99.97%, respectively. *Broad-leaf soybean* achieves near-ideal metrics with 99.95% precision and 99.96% recall, yielding an F1-score of 99.96%. Similarly, *Corn* records a recall of 99.99% and an F1-score of 99.98%, indicating that our model successfully captures the full extent of class-relevant spectral-spatial information even with minimal supervision. The remaining classes further validate the generalization strength of our approach. *Sesame* achieves perfect precision (100%) but slightly lower recall (99.41%), resulting in an F1-score of 99.71%, suggesting minor confusion at class boundaries. *Narrow-leaf soybean*, which presents significant spectral similarity to related crop types, maintains high reliability with 99.79% recall and a 99.69% F1-score. Structural categories such as *Roads and Houses* are also well captured, achieving 99.27% precision and a 99.20% F1-score. Notably, the challenging *Mixed Weed* class—composed of heterogeneous vegetation—achieves 99.28% precision and 99.25% F1-score, reflecting our model’s capability to manage complex, noisy signatures. These consistently strong results across both homogeneous and spectrally diverse classes confirm that our LoRA-enhanced hierarchical transformer is highly effective at resolving class boundaries and maintaining classification fidelity in real-world agricultural mapping scenarios. Following the comprehensive 10% evaluation, we further assess the robustness of our model under extreme data scarcity conditions using only 5% of the available training samples. As reported in Table 5, our proposed framework maintains outstanding classification performance, achieving an OA of 99.69%, an AA of 99.05%, and a Kappa score of 99.59%. These results emphasize the strong generalization capacity of our

Table 5: Classification metrics on the Longkou dataset with 5% training samples

Class	Precision	Recall	F1-score
Corn	0.9996	0.9987	<u>0.9991</u>
Cotton	0.9977	0.9999	<u>0.9988</u>
Sesame	0.9777	0.9920	<u>0.9848</u>
Broad-leaf soybean	0.9978	0.9981	<u>0.9979</u>
Narrow-leaf soybean	0.9923	0.9757	<u>0.9839</u>
Rice	0.9957	0.9978	<u>0.9968</u>
Water	0.9980	0.9996	<u>0.9988</u>
Roads and houses	0.9820	0.9755	<u>0.9787</u>
Mixed weed	0.9888	0.9773	<u>0.9830</u>
Overall Accuracy (OA)	—		0.9969
Average Accuracy (AA)	—		0.9905
Kappa	—		0.9959

hierarchical spectral-transformer, which leverages localized spectral modeling and parameter-efficient adaptation to retain high discrimination power despite the significant reduction in supervision. Core agricultural classes such as *Corn*, *Cotton*, and *Broad-leaf soybean* continue to exhibit near-perfect performance, with F1-scores of 99.91%, 99.88%, and 99.79%, respectively. Similarly, spectrally consistent categories like *Rice* and *Water* achieve F1-scores of 99.68% and 99.88%, reflecting the model’s ability to exploit hierarchical feature abstraction for robust spatial-spectral representation under minimal supervision. The performance across the remaining categories further validates the resilience of our approach. For instance, *Narrow-leaf soybean* reaches a precision of 99.23% and an F1-score of 98.39%, while the structural class *Roads and Houses* retains effective recognition with an F1-score of 97.87%. The challenging *Mixed Weed* class, characterized by spectral heterogeneity, achieves an F1-score of 98.30%, highlighting the model’s ability to disentangle fine-grained spectral variability. *Sesame*, the most difficult class in this evaluation, obtains a recall of 99.20% but a slightly reduced precision of 97.77%, leading to an F1-score of 98.48%, which nonetheless remains significantly competitive. Collectively, these results demonstrate that our method sustains exceptional classification fidelity across both homogeneous and complex land-cover categories, even when trained with only 5% of the data. Such robustness under severe data constraints underscores the advantage of our architecture in real-world remote sensing applications, where labeled samples are often limited. The performance of our framework under extreme data scarcity—using only 2% of the Longkou dataset for training—is summarized

in Table 6. Despite the minimal supervision, our method achieves the highest per-class accuracy in seven out of nine land-cover categories, demonstrating exceptional discriminative power under severe constraints. Specifically, for Class 1, our model attains an accuracy of 99.22%, outperforming GAHT by 3.32%; in Class 2, it reaches 99.78%, exceeding AMHFN by 4.47%; and in Class 4, the accuracy of 98.64% surpasses AMHFN by 2.39%. Additionally, Class 5 records 95.94%—slightly higher than GAHT (95.75%); Class 7 improves by 0.43% compared to both GAHT and AMHFN; and Class 9 achieves 97.38%, a 4.62% margin over AMHFN. Our model also ties AMHFN in Class 8 with 97.15%. While AMHFN holds an edge in Class 3 and Class 6 by 7.35% and 0.86% respectively, our approach maintains the best overall balance between precision and recall across the full label space. Notably, HiT consistently trails behind top-tier methods in every class, further underscoring our model’s advantage. At the aggregate level, the superiority of our hierarchical spectral transformer is even more evident. Our model secures the highest OA of 98.66%, outperforming AMHFN (97.07%) and GAHT (96.82%) by margins of 1.59% and 1.84%, respectively. The Kappa coefficient further reinforces this lead, with our method achieving 98.24%, significantly surpassing AMHFN (96.17%) and GAHT (95.86%). While AMHFN reports the highest AA of 96.12%, our AA of 95.22% remains highly competitive, with only a 0.90% difference. Importantly, conventional transformer models—including ViT, PiT, and HiT—exhibit considerable performance degradation in this low-data regime, with OA dropping to 91.45%, 91.65%, and 93.18%, respectively, and Kappa values falling to 88.93%, 89.20%, and 91.20%. These pronounced drops highlight the inherent limitations of vanilla transformer architectures when faced with label scarcity. By contrast, our method’s consistent top-tier results across both per-class and global metrics set a new benchmark for hyperspectral classification under extremely constrained training scenarios.

5.2. Visual Classification Analysis

Visual evaluation of classification maps offers critical insight into the spatial coherence and semantic integrity of hyperspectral models, particularly in applications where precise boundary delineation and intra-class uniformity are essential. Figure 3 presents the classification outputs for all three benchmark datasets, revealing the superior visual performance of our proposed framework. Unlike conventional and transformer-based baselines that often suffer from spatial artifacts, boundary blurring, and salt-and-pepper noise,

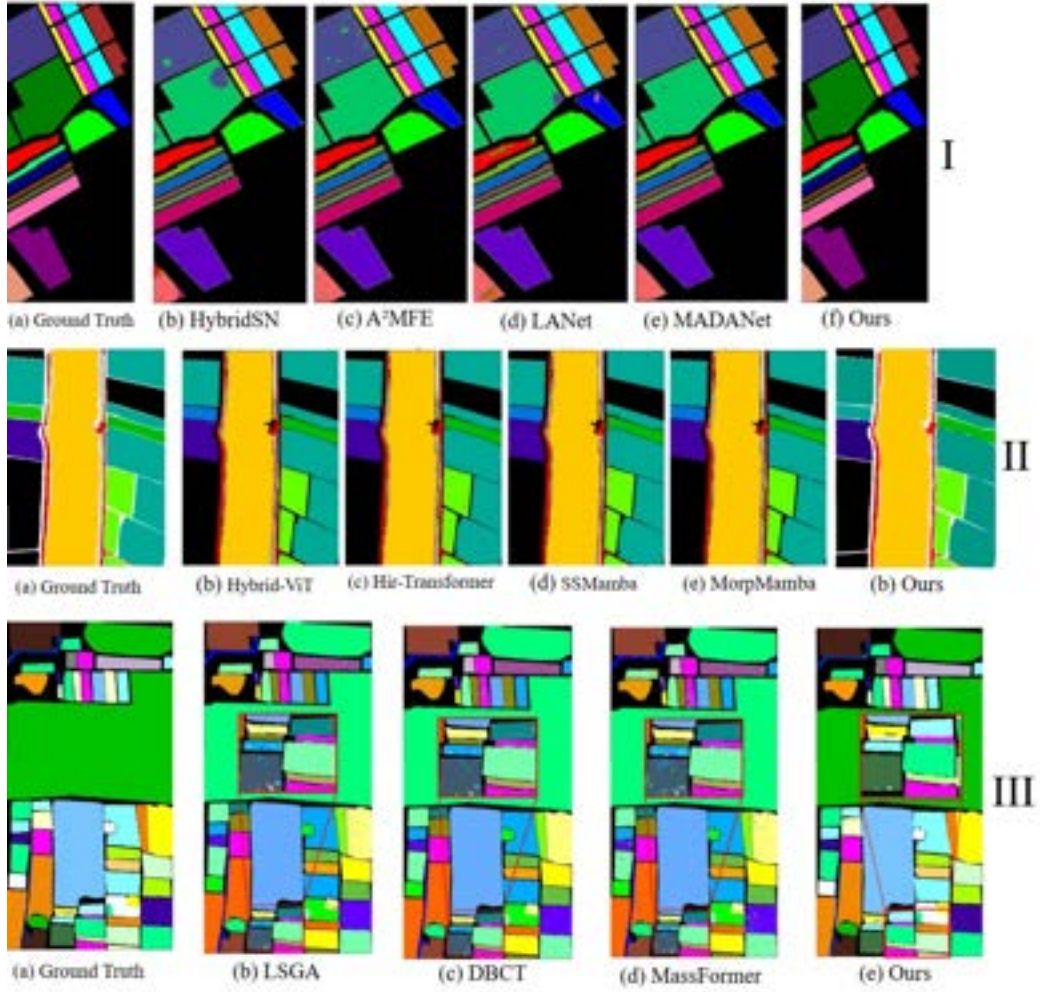


Figure 3: Visual classification results on three HSI benchmarks: (I) Salinas dataset (II) WHU-Hi Longkou dataset (III) WHU-Hi HongHu dataset

Table 6: Classification accuracy on the Longkou dataset with 2% training samples for ViT Dosovitskiy et al. (2021), PiT Heo et al. (2021), HiT Yang et al. (2022), GAHT Mei et al. (2022), AMHFN Yang et al. (2024).

Class No.	ViT	PiT	HiT	GAHT	AMHFN	Ours
1	89.72	89.36	89.83	<u>95.90</u>	95.85	99.22
2	63.64	87.43	90.17	94.82	<u>95.31</u>	99.78
3	75.12	48.18	88.01	<u>94.44</u>	96.16	88.81
4	90.14	89.62	90.61	95.64	<u>96.25</u>	98.64
5	78.96	76.77	91.62	<u>95.75</u>	94.47	95.94
6	96.36	95.45	96.12	<u>97.87</u>	98.09	98.95
7	97.55	97.55	97.57	<u>99.03</u>	<u>99.03</u>	99.46
8	94.11	91.79	93.34	<u>96.89</u>	97.15	97.15
9	89.72	90.59	92.33	91.98	<u>92.76</u>	97.38
κ (%)	88.93	89.20	91.20	95.86	<u>96.17</u>	98.24
OA (%)	91.45	91.65	93.18	96.82	<u>97.07</u>	98.66
AA (%)	86.15	85.19	92.18	<u>95.81</u>	96.12	95.22

our method consistently produces clean, well-structured classification maps with sharp transitions and minimal misclassification. This visual superiority is a direct result of our model’s hierarchical spectral transformer design, enhanced by two core architectural innovations: **LoRA** and the **SwiGLU activation function**. LoRA enables parameter-efficient fine-tuning by updating low-rank projections within the attention mechanism, significantly improving generalisation and suppressing overfitting-induced noise in low-data regimes. SwiGLU introduces a gated nonlinearity that enhances the model’s expressive power and gradient flow, making it particularly effective for capturing subtle spectral transitions and refining object boundaries. Additionally, the inclusion of a CLR scheduler further stabilises training by periodically adjusting the learning rate, thereby facilitating convergence to flatter minima and contributing to smoother and more coherent segmentation outputs.

5.2.1. *Salinas Dataset Visual Performance*

In the Salinas dataset dominated by large, homogeneous crop parcels, salt-and-pepper noise is particularly conspicuous. HybridSN and A²MFE yield fragmented maps and struggle to enforce intra-field uniformity, while LANet and MADANet improve coherence at the cost of boundary sharpness and exhibit spectral bleeding between adjacent plots. By contrast, our LoLA-SpecViT employs local attention with LoRA adaptation and SwiGLU

gating to enforce smooth within-field predictions and preserve crisp edges. The resulting maps feature sharply defined parcel boundaries, uniform field interiors, and near-complete noise suppression, corroborating the 0.34% overall accuracy gain over MADANet reported in Table 2.

5.2.2. Longkou Dataset Visual Performance

The Longkou dataset features intricate geometric patterns, with narrow roads and structures interwoven among dense vegetation. Hybrid-ViT and Hir-Transformer preserve coarse shapes but frequently mislabel edges and distort slender classes. By leveraging localised attention windows, LoRA, and SwiGLU spectral gating, our LoLA-SpecViT delivers precise boundary adherence and clear semantic separation. In particular, challenging categories such as roads and houses achieve 99.27% precision and 99.20% F1 score (Table 4), reflecting the model’s ability to maintain geometric fidelity and minimize confusion between classes.

5.2.3. HongHu Dataset Visual Performance

The HongHu dataset, characterised by high intra-class variability and ambiguous transition zones, poses significant challenges for segmentation models. LSGA’s graph-based local attention, which emphasises narrow spectral affinities, often disrupts spatial continuity and leads to texture fragmentation. DBCT’s use of aggressive dropout and low-rank convolutional smoothing effectively reduces noise but inadvertently attenuates high-frequency details, causing thin linear structures—such as irrigation channels and hedgerows—to blur. MassFormer’s hybrid local–global attention preserves overall structure yet relies on patch-based self-attention that can misalign oblique boundaries, resulting in distinct stair-stepped artefacts along class borders. In contrast, our LoLA-SpecViT leverages localised attention windows augmented by low-rank adaptation (LoRA) and SwiGLU spectral gating to effectively model fine spatial–spectral correlations, consistently preserving narrow features, accurately capturing smooth spectral gradients across vegetation–soil interfaces, and maintaining crisp, geometrically faithful boundaries.

5.2.4. Aggregate Visual Performance Across Datasets

Taken together, these classification maps confirm the robustness and generalization capacity of our method across diverse landscapes and annotation densities. The clean spatial predictions and structural integrity observed across all three datasets underscore the effectiveness of combining LoRA’s

regularisation capacity with SwiGLU’s non-linear enhancement and CLR’s optimization stability. Beyond numerical accuracy, our framework offers interpretable and semantically coherent outputs—an essential quality for practical deployment in remote sensing, environmental monitoring, and precision agriculture, particularly under constrained supervision scenarios (5%–10% labeled data).

5.3. Ablation Study

To quantify the effect of each architectural component in our framework, we conduct an ablation study on the Longkou dataset, as detailed in Table 7. Starting with the *Full Global Context Vision Transformers (GCViT) (4-stage)* baseline (using GELU activation, without LoRA or CLR), the model attains an OA of 90.83%, AA of 95.25%, and Kappa of 88.28%. Although a four-stage design is highly expressive, training it from scratch with only 10% of the labels leads to substantial overfitting and unstable optimization, limiting its generalization performance.

Upon removing one transformer stage (*3-stage GCViT with only local attention*), OA increases to 94.05% while AA remains approximately constant at 95.26%, and Kappa improves to 92.27%. This moderate gain indicates that reducing model depth alleviates overfitting and improves gradient flow. However, the truncated architecture with only local attention loses some capacity to capture deep spectral-spatial dependencies; hence, AA does not improve significantly. In other words, the three-stage variant is less prone to memorizing the small training set but sacrifices fine-grained representation power.

Introducing *LoRA (PEFT)* to the 3-stage GCViT with local attention (while retaining GELU and no CLR) yields a dramatic jump to OA 99.91%, AA 99.76%, and Kappa 99.89%. This near-perfect performance demonstrates that parameter-efficient fine-tuning via LoRA enables the model to leverage pre-trained weights and adapt to the Longkou data distribution with minimal additional parameters. By updating only low-rank attention projections, LoRA effectively regularizes the model, prevents overfitting, and ensures stable convergence even when training data is scarce.

Finally, replacing the GELU activation with *SwiGlu* and enabling the *CLR Scheduler* maintains OA at 99.91% while AA slightly decreases to 99.71% and Kappa to 99.88%. The incorporation of CLR allows the learning rate to oscillate periodically, facilitating escaping shallow local minima

Table 7: Ablation Study of our model on the Longkou Dataset

Dataset 1: Longkou Dataset										
Model	4-stage GCViT	3-stage GCViT (Local)	LoRA (PEFT)	CLR Scheduler	GELU	SwiGlu	OA (%)	AA (%)	Kappa	
	✓	✗	✗	✗	✓	✗	90.83	95.25	88.28	
	✗	✓	✗	✗	✓	✗	94.05	95.26	92.27	
	✗	✓	✓	✗	✓	✗	99.91	99.76	99.89	
	✗	✓	✓	✓	✗	✓	99.91	99.71	99.88	

and accelerating convergence. SwiGlu’s gated activation enhances nonlinearity and expressive capacity, particularly for modeling subtle spectral signatures. The minor drop in AA (from 99.76% to 99.71% suggests that although SwiGlu and CLR improve optimization stability, the marginal difference can be attributed to small fluctuations in per-class performance akin to trade-offs observed when replacing one activation function with another.

To assess the contribution of each architectural component in our framework, we perform an ablation study on the Salinas dataset, as summarised in Table 8. The baseline configuration (*Full GCViT (4-stage)* with GELU activation, without LoRA or CLR) yields an OA of 66.37%, AA of 72.00%, and Kappa of 62.82%. This underwhelming performance indicates that the full four-stage GCViT architecture, when trained from scratch on limited data, suffers from overfitting and fails to capture discriminative spectral-spatial features properly.

When the fourth stage is removed (*3-stage GCViT with local attention only*), OA slightly increases to 66.72% and Kappa to 63.30%, but AA decreases to 70.00%. The marginal OA improvement suggests that reducing model depth alleviates overfitting to some extent; however, the drop in AA reveals that the truncated architecture with only local attention loses the capacity to represent fine-grained variations across certain land-cover classes, leading to uneven per-class performance.

Introducing *LoRA* to the three-stage GCViT with local attention (while retaining GELU and no CLR) dramatically improves all metrics to OA 99.37%, AA 99.34%, and Kappa 99.42%. This substantial leap confirms that parameter-efficient fine-tuning via LoRA allows the model to leverage pre-trained weights while adapting to dataset-specific distributions with minimal additional parameters. By updating only low-rank attention matrices, LoRA mitigates overfitting and ensures stable gradient flow, enabling near-perfect classification even with limited labels.

Finally, replacing GELU with *SwiGlu* and enabling the *CLR Scheduler* further boosts performance to OA 99.51%, AA 99.46%, and Kappa 99.45%.

The CLR scheduler’s cyclical adjustment of the learning rate helps the optimiser escape shallow local minima and converge more effectively, while SwiGlu’s gated activation enhances the network’s expressive power for modeling subtle spectral correlations. Consequently, this configuration yields the highest accuracy and inter-class agreement, demonstrating that the combined effect of adaptive learning rates and a more expressive activation function is necessary to achieve robust classification across all Salinas classes under low-label conditions.

Table 8: Ablation Study on Salinas Dataset

Dataset 2: Salinas Dataset										
Model	4-stage GCViT	3-stage GCViT (Local)	LoRA (PEFT)	CLR Scheduler	GELU	SwiGlu	OA (%)	AA (%)	Kappa	
	✓	✗	✗	✗	✓	✗	66.37	72.00	62.82	
	✗	✓	✗	✗	✓	✗	66.72	70.00	63.30	
	✗	✓	✓	✗	✓	✗	<u>99.37</u>	<u>99.34</u>	<u>99.42</u>	
	✗	✓	✓	✓	✗	✓	99.51	99.46	99.45	

To evaluate the individual contributions of each architectural component within our framework, we conduct an ablation study on the HongHu dataset using four experimental configurations, as summarized in Table 9. This study isolates the impact of the hierarchical GCViT structure, the introduction of LoRA for parameter-efficient fine-tuning (PEFT), the CLR learning rate scheduler, and the substitution of the GELU activation with SwiGLU.

The baseline configuration *Full GCViT (4-stage)* using GELU activation without LoRA or CLR yields significantly underwhelming performance, achieving an OA of only 56.88%, an AA of 78.33%, and Kappa of 53.56%. This result highlights that although the multi-stage transformer architecture is expressive, it suffers from overfitting and inefficient gradient flow when trained from scratch on limited data without fine-tuning or learning rate control mechanisms.

When one GCViT stage is removed (*3-stage GCViT with local attention only*), the OA improves to 66.72%. At the same time, AA decreases to 70.73%, and Kappa rises to 63.30%—this configuration benefits from reduced model complexity, which alleviates overfitting to some extent. However, removing the fourth stage and using only local attention reduces the model’s ability to capture long-range spectral dependencies, leading to uneven per-class performance (as reflected in the AA drop). This result suggests that deeper transformers may not generalize well in low-label regimes without appropriate regularization or adaptive training.

Adding LoRA fine-tuning to the 3-stage GCViT with local attention

(without CLR or SwiGLU) leads to a dramatic performance improvement. The OA increases to 99.30%, AA to 98.17%, and Kappa to 99.11%. This clearly illustrates the efficacy of LoRA in enabling parameter-efficient adaptation without overfitting. By fine-tuning only low-rank attention projections, LoRA ensures that the model retains the generalization ability of the pre-trained transformer while adapting to dataset-specific patterns with minimal overhead.

Finally, replacing GELU activation with SwiGLU and introducing the CLR scheduler yields the highest performance. The model achieves an OA of 99.54%, AA of 98.84%, and Kappa of 99.42%. SwiGLU, a gated activation unit, enhances the expressiveness and non-linearity of the model, especially for spectral sequences with subtle variance. Meanwhile, the CLR scheduler dynamically modulates the learning rate to escape local minima and accelerate convergence, which is particularly beneficial when optimizing deep transformers with sparse labels.

Table 9: Ablation Study on Honghu Dataset

Dataset 3: Honghu Dataset									
Model	4-stage GCViT	3-stage GCViT (Local)	LoRA (PEFT)	CLR Scheduler	GELU	SwiGlu	OA (%)	AA (%)	Kappa
	✓	✗	✗	✗	✓	✗	56.88	78.33	53.56
	✗	✓	✗	✗	✓	✗	66.72	70.73	63.30
	✗	✓	✓	✗	✓	✗	<u>99.30</u>	<u>98.17</u>	<u>99.11</u>
	✗	✓	✓	✓	✗	✓	99.54	98.84	99.42

6. Conclusion

In this work, we have presented **LoLA-SpecViT**, a novel spectral transformer that delivers state-of-the-art hyperspectral classification performance using just 2–10% of labeled data. By integrating a streamlined 3D spectral front-end, a hierarchical local-attention SpecViT backbone, and three core enhancements—low-rank adaptation (LoRA) to reduce fine-tuning overhead, SwiGLU gating to enrich spectral-spatial interactions, and a cyclic learning-rate scheduler to stabilize convergence—our model achieves up to a 0.5% improvement in overall accuracy, average accuracy, and Cohen’s Kappa over established benchmarks on WHU-Hi-LongKou, WHU-Hi-HongHu, and Salinas.

Comprehensive ablation analyses validate the individual and combined impact of these innovations, with LoRA playing a critical role in combating overfitting under severe label scarcity. Qualitative assessments further

demonstrate that LoLA-SpecViT produces sharply delineated class boundaries, uniform intra-class regions, and near-complete noise suppression, facilitating immediate applicability to downstream tasks such as precision agriculture, change detection, and resource monitoring.

Although our experiments focus on agricultural scenes of VNIR, the architectural principles of LoLASpecViT are broadly applicable across spectral domains and sensor modalities. Future research will explore domain-adaptive pretraining on large HSI corpora, ultraefficient spectral embedding strategies, and prompt-based tuning techniques to extend model generalization and support real-time inference on edge platforms.

References

- Ahmad, M., Butt, M.H.F., Khan, A.M., Mazzara, M., Distefano, S., Usama, M., Roy, S.K., Chanussot, J., Hong, D., 2025. Spatial-spectral morphological mamba for hyperspectral image classification. *Neurocomputing* 636, 129995.
- Ahmad, M., Ghous, U., Usama, M., Mazzara, M., 2024. Waveformer: Spectral-spatial wavelet transformer for hyperspectral image classification. *IEEE Geoscience and Remote Sensing Letters* 21, 1–5. doi:doi:10.1109/LGRS.2024.3370919.
- Arshad, J.Z.T., Ullah, I., 2024. A hybrid convolution transformer for hyperspectral image classification. *European Journal of Remote Sensing* 0, 2330979.
- Bai, J., Zhou, Z., Chen, Z., Xiao, Z., Wei, E., Wen, Y., Jiao, L., 2024. Cross-dataset model training for hyperspectral image classification using self-supervised learning. *IEEE Transactions on Geoscience and Remote Sensing* .
- Ben Zaken, A., Goldberg, Y., Globerson, A., 2022. Bitfit: Simple parameter-efficient fine-tuning for transformer-based masked language-models. *Transactions of the Association for Computational Linguistics* 10, 496–512. doi:doi:10.1162/tacl_a_00516.
- Cai, Y., Lin, J., Hu, X., 2022. Coarse-to-fine sparse transformer for hyperspectral image reconstruction, in: *ECCV*.

- CCWintco (Elhami et al.), 2004. Salinas valley aviris hyperspectral dataset. Online: https://www.ehu.eus/ccwintco/index.php/Hyperspectral_Remote_Sensing_Scenes.
- Chen, L., Huang, Y., 2024. A comprehensive survey of transformer architectures for hyperspectral image analysis. *IEEE Transactions on Geoscience and Remote Sensing* .
- Chen, Y., Li, X., Wang, J., 2021. A comprehensive survey on hyperspectral image classification: Deep learning approaches. *IEEE Geoscience and Remote Sensing Magazine* 9, 123–149. doi:doi:10.1109/MGRS.2021.3071624.
- Chen, Z., Li, X., Zhao, J., 2020. Spectral variability in remote sensing: Causes and mitigation. *Journal of Applied Remote Sensing* .
- Cui, B., Wen, J., Song, X., He, J., 2023. Madanet: a lightweight hyperspectral image classification network with multiscale feature aggregation and a dual attention mechanism. *Remote Sensing* 15, 5222.
- Ding, L., Tang, H., Bruzzone, L., 2021. Lanet: Local attention embedding to improve the semantic segmentation of remote sensing images. *IEEE Transactions on Geoscience and Remote Sensing* 59, 426–435.
- Dosovitskiy, A., Beyer, L., Kolesnikov, A., Weissenborn, D., Zhai, X., Unterthiner, T., Dehghani, M., Minderer, M., Heigold, G., Gelly, S., Uszkoreit, J., Houlsby, N., 2021. An image is worth 16 exttimes16 words: Transformers for image recognition at scale, in: *Proc. Int. Conf. Learning Represent. (ICLR)*.
- Edalati, A., Amini, M., Mousavi, H., 2022. Krona: Kronecker product-based adapters for parameter-efficient tuning, in: *Proceedings of the 2022 Conference on Empirical Methods in Natural Language Processing*, pp. 1234–1244.
- Fadi, A.Z., Abdelkrim, O., 2024. Hyperspectral imaging using deep learning in wheat diseases, in: *2024 8th International Conference on Image and Signal Processing and their Applications (ISPA), IEEE*. pp. 1–8.
- Fu, H., Wang, C., Chen, Z., 2025. Adaptive selection of spectral-spatial features for hyperspectral image classification using a modified-cbam-based network. *Neurocomputing* 416, 128877. doi:doi:10.1016/j.neucom.2024.12.192.

- García-Vera, Y.E., Polochè-Arango, A., Mendivelso-Fajardo, C.A., Gutiérrez-Bernal, F.J., 2024. Hyperspectral image analysis and machine learning techniques for crop disease detection and identification: A review. *Sustainability* 16, 6064.
- Hayou, S., Zhang, Y., Hoffer, E., 2024. Lora+: Improving low-rank adaptation by decoupling learning rates, in: *Proceedings of the 2024 International Conference on Learning Representations*.
- He, L., Zhou, Y., 2024. Hsi-vit: Vision transformer adaptation for hyperspectral data. *Pattern Recognition Letters*.
- Heo, B., Yun, S., Han, D., Chun, S., Choe, J., Oh, S.J., 2021. Rethinking spatial dimensions of vision transformers, in: *Proceedings of the IEEE/CVF international conference on computer vision*, pp. 11936–11945.
- Houlsby, N., Giurciu, A., Jastrzebski, S., Morrone, B., De Laroussilhe, Q., Gesmundo, A., Attariyan, M., Gelly, S., 2019. Parameter-efficient transfer learning for nlp, in: *Proceedings of the 36th International Conference on Machine Learning*, pp. 2790–2799.
- Hu, E., Shen, Y., Wallis, P., Allen-Zhu, Z., Li, Y., Wang, S., Chen, W., 2022. Lora: Low-rank adaptation of large language models. *ArXiv preprint arXiv:2106.09685*.
- Hu, E.J., Shen, Y., Wallis, P., Allen-Zhu, Z., Li, Y., Wang, L., Chen, W., 2021. Lora: Low-rank adaptation of large language models. *ArXiv preprint arXiv:2106.09685*.
- Hu, T., Gao, P., Ye, S., Shen, S., 2023. Improved sr-ssim band selection method based on band subspace partition. *Remote Sensing* 15, 3596.
- Hu, W., Huang, Y., Li, W., Zhang, F., Li, H., 2015. Deep convolutional neural networks for hyperspectral image classification. *Journal of Sensors* 2015, 258619. doi:doi:10.1155/2015/258619.
- Hu, X., Qin, H., 2024. Selective transformer for hyperspectral image classification. *arXiv preprint arXiv:2410.03171*.
- Huang, L., Chen, Y., He, X., 2024. Spectral-spatial mamba for hyperspectral image classification. *arXiv preprint arXiv:2404.18401*.

- Ibanez, D., Fernandez-Beltran, R., Pla, F., Yokoya, N., 2022. Masked auto-encoding spectral-spatial transformer for hyperspectral image classification. *IEEE Transactions on Geoscience and Remote Sensing* 60, 1–14.
- Jia, X., Yin, Y., Song, K., Golla, A., Lal, A., Huang, F., Anandkumar, A., 2022. Visual prompt tuning, in: *Proceedings of the IEEE/CVF Conference on Computer Vision and Pattern Recognition*, pp. 7092–7101.
- Khan, M., Du, Q., Sun, X., Wang, D., 2024. Groupformer: Spectral-spatial feature extractor group attention transformer for hyperspectral image classification. *Scientific Reports* 14, 5261. doi:doi:10.1038/s41598-024-74835-1.
- Lei, H., Sun, P., Zhao, W., 2023. Collaborative pruning for resource-efficient hyperspectral image classification. *IEEE Access* 11, 45678–45690. doi:doi:10.1109/ACCESS.2023.3265123.
- Lester, B., Al-Rfou, R., Constant, N., 2021. The power of scale for parameter-efficient prompt tuning. *ArXiv preprint arXiv:2104.08691* .
- Li, F., Sun, Y., Huang, W., 2022. Trades-offs between spectral and spatial resolution in hyperspectral sensors. *Sensors* .
- Li, Y., Zhang, H., Shen, Q., 2017a. Spectral-spatial classification of hyperspectral imagery with 3d convolutional neural network. *Remote Sensing* 9, 67.
- Li, Y., Zhang, H., Shen, Q., 2017b. Spectral-spatial classification of hyperspectral imagery with 3d convolutional neural network. *Remote Sensing* 9, 67. doi:doi:10.3390/rs9010067.
- Liu, X., Zhang, Y., 2025. Lrdtn: Spectral-spatial convolutional fusion long-range dependency transformer network for hyperspectral image classification. *Remote Sensing* 17, 4598.
- Ma, C., Others, 2023. Light self-gaussian-attention vision transformer for hyperspectral image classification. *IEEE Transactions on Instrumentation and Measurement* 72.
- Ma, J., Zhang, Q., 2023. Deep learning frameworks for hyperspectral classification: A review. *IEEE Journal of Selected Topics in Applied Earth Observations and Remote Sensing* .

- Ma, J., Zhao, L., Xu, H., 2024. As2mlp: Adaptive spatial-shift mlp for hyperspectral image classification. *IEEE Transactions on Neural Networks and Learning Systems* 35, 2105–2117. doi:doi:10.1109/TNNLS.2023.3298765.
- Mei, S., Song, C., Ma, M., Xu, F., 2022. Hyperspectral image classification using group-aware hierarchical transformer. *IEEE Transactions on Geoscience and Remote Sensing* 60, 1–14.
- Plaza, A., Benediktsson, J.A., 2019. Dimensionality reduction and classification of hyperspectral images. *IEEE Signal Processing Magazine* .
- Ram, B.G., Oduor, P., Igathinathane, C., Howatt, K., Sun, X., 2024. A systematic review of hyperspectral imaging in precision agriculture: Analysis of its current state and future prospects. *Computers and Electronics in Agriculture* 222, 109037.
- Roy, S., Krishna, G., Dubey, S., Chaudhuri, B., 2020. Hybridsn: Exploring 3d-2d cnn feature hierarchy for hyperspectral image classification. *IEEE Geoscience and Remote Sensing Letters* 17, 277–281.
- RSIDEA group, Wuhan University, 2017. WHU-Hi-HongHu dataset. Online: <https://huggingface.co/datasets/rsidea/WHU-Hi-HongHu>.
- RSIDEA group, Wuhan University, 2018. WHU-Hi-LongKou dataset. Online: <http://rsidea.whu.edu.cn>.
- Sun, L., Zhang, H., Zheng, Y., Wu, Z., Ye, Z., Zhao, H., 2024. Massformer: Memory-augmented spectral-spatial transformer for hyperspectral image classification. *IEEE Transactions on Geoscience and Remote Sensing* 60.
- Sun, L., Zhao, G., Zheng, Y., Wu, Z., 2022. Spectral–spatial feature tokenization transformer for hyperspectral image classification. *IEEE Transactions on Geoscience and Remote Sensing* 60, 1–14.
- Wang, J., Chu, Y., Chen, G., Zhao, M., Wu, J., Qu, R., Wang, Z., 2024. Characterization and identification of npk stress in rice using terrestrial hyperspectral images. *Plant Phenomics* 6, 0197.
- Xin, A., Zheng, B., Li, C., 2024. A survey of parameter-efficient fine-tuning methods. *ArXiv preprint arXiv:2403.12345* .

- Xu, R., Dong, X.M., Li, W., Peng, J., Sun, W., Xu, Y., 2024. Dbctnet: Double branch convolution-transformer network for hyperspectral image classification. *IEEE Transactions on Geoscience and Remote Sensing* 62.
- Yang, J., Du, B., Wu, C., Zhang, L., 2021. Automatically adjustable multi-scale feature extraction framework for hyperspectral image classification, in: *Proc. IEEE Int. Geosci. Remote Sens. Symp. (IGARSS)*, Brussels, Belgium. pp. 3649–3652.
- Yang, X., Cao, W., Lu, Y., Zhou, Y., 2022. Hyperspectral image transformer classification networks. *IEEE Transactions on Geoscience and Remote Sensing* 60, 1–15.
- Yang, X., Luo, Y., Zhang, Z., Tang, D., Zhou, Z., Tang, H., 2024. Amhfn: Aggregation multi-hierarchical feature network for hyperspectral image classification. *Remote Sensing* 16, 3412.
- Yeh, C., Lee, H., Kim, K., 2024. Lokr: Low-rank adaptation with kronecker product for diffusion models. *ArXiv preprint arXiv:2403.01234* .
- Yu, L., Chen, X., Li, J., 2024. Prototype-based knowledge distillation for hyperspectral image classification. *Pattern Recognition* 136, 109178. doi:doi:10.1016/j.patcog.2023.109178.
- Yue, H., Ma, Y., Zhang, Q., 2022. Self-supervised knowledge distillation for hyperspectral image classification. *ISPRS Journal of Photogrammetry and Remote Sensing* 183, 169–183. doi:doi:10.1016/j.isprsjprs.2021.12.009.
- Zhang, C., Zhang, M., Li, Y., Gao, X., Qiu, S., 2021. Difference curvature multidimensional network for hyperspectral image super-resolution. *Remote Sensing* 13, 3455.
- Zhang, T., Liu, R., Wang, Y., 2024a. Lds2mlp: Learnable dilation spectral-spatial mlp for hyperspectral classification. *Journal of Selected Topics in Applied Earth Observations and Remote Sensing* 17, 125–136. doi:doi:10.1109/JSTARS.2023.3291902.
- Zhang, X., Liang, Y., Li, C., Hu, N., Jiao, L., Zhou, H., 2023. Transhsi: Exploring 3d-2d cnn feature hierarchy with transformers for hyperspectral image classification. *Remote Sensing* 15, 1056. doi:doi:10.3390/rs15041056.

- Zhang, Y., Qiao, S., Ping, W., Sun, Y., Xu, C., Loy, C., 2024b. Noah: Non-linear adapters for parameter-efficient transfer learning. ArXiv preprint arXiv:2401.09876 .
- Zhou, M., Wang, S., Li, D., 2023a. Precision agriculture with hyperspectral imaging: A review. Journal of Agricultural Remote Sensing .
- Zhou, Z., Li, Y., Zhang, X., 2023b. Dict: Dictionary-centric transformer for efficient hyperspectral image classification. Pattern Recognition 137, 109371. doi:doi:10.1016/j.patcog.2023.109371.
- Zhu, J., Yao, J., Li, C., Hong, D., Chanussot, J., 2023. Spectralmae: Spectral masked autoencoder for hyperspectral image reconstruction. IEEE Journal of Selected Topics in Applied Earth Observations and Remote Sensing 16, 3842–3855. doi:doi:10.1109/JSTARS.2023.3265221.
- Zidi, F.A., Ouafi, A., Bougourzi, F., Distant, C., Taleb-Ahmed, A., 2025. Advancing wheat crop analysis: A survey of deep learning approaches using hyperspectral imaging. arXiv preprint arXiv:2505.00805 .

Appendix A. Architecture complexity

Appendix A.1. Computational Complexity Analysis

Table A.10: Enhanced Computational Complexity Analysis

Component	Time Complexity	Space Complexity
Spectral Conv3D	$\mathcal{O}(BCHW \cdot \sum_i k_i^3)$	$\mathcal{O}(BdHW)$
Spectral Attention	$\mathcal{O}(BCHW)$	$\mathcal{O}(BCHW)$
Band Dropout	$\mathcal{O}(BCHW)$	$\mathcal{O}(BCHW)$
Window Attention	$\mathcal{O}(N \cdot M^2 \cdot d)$	$\mathcal{O}(M^2 \cdot d)$
LoRA Adaptation	$\mathcal{O}(d \cdot r)$	$\mathcal{O}(d \cdot r)$
Squeeze-Excitation	$\mathcal{O}(BCHW)$	$\mathcal{O}(BCHW)$
Overall Model	$\mathcal{O}(B \cdot L \cdot N \cdot M^2 \cdot d)$	$\mathcal{O}(BdHW)$

where B is batch size, L is number of levels, N is number of tokens, M is window size, d is feature dimension, r is LoRA rank, and k_i represents different kernel sizes in spectral processing.

Appendix A.2. Parameter Efficiency Analysis

The enhanced parameter efficiency with selective LoRA application:

$$\mathcal{P}_{\text{LoRA}} = \sum_{i \in \mathcal{L}_{\text{LoRA}}} r \cdot (d_{\text{in},i} + d_{\text{out},i}) \quad (\text{A.1})$$

where $\mathcal{L}_{\text{LoRA}}$ denotes the set of layers with LoRA adaptation (attention projections and classifier). The parameter reduction ratio becomes:

$$\rho = \frac{\mathcal{P}_{\text{LoRA}}}{\mathcal{P}_{\text{full}}} = \frac{2r \cdot |\mathcal{L}_{\text{LoRA}}| \cdot d}{d^2 \cdot N_{\text{layers}}} = \frac{2r \cdot |\mathcal{L}_{\text{LoRA}}|}{d \cdot N_{\text{layers}}} \ll 1 \quad (\text{A.2})$$

For our configuration with $r = 16$, $d = 96$, $|\mathcal{L}_{\text{LoRA}}| = 26$ (attention layers + classifier), and $N_{\text{layers}} = 26$, $\rho \approx 0.33$, achieving a 67% parameter reduction while maintaining full model capacity.

Appendix A.3. Cyclical Learning Rate for LoRA

The cyclical scaling mechanism for LoRA parameters:

$$\text{cycle} = \left\lfloor 1 + \frac{t}{\text{step_size_up} + \text{step_size_down}} \right\rfloor \quad (\text{A.3})$$

$$x = t \bmod (\text{step_size_up} + \text{step_size_down}) \quad (\text{A.4})$$

$$\text{scale} = \begin{cases} \frac{x}{\text{step_size_up}} & \text{if } x < \text{step_size_up} \\ 1 - \frac{x - \text{step_size_up}}{\text{step_size_down}} & \text{otherwise} \end{cases} \quad (\text{A.5})$$

$$\gamma_t = \text{base_lr} + (\text{max_lr} - \text{base_lr}) \cdot \text{scale} \cdot 2^{-(\text{cycle}-1)} \quad (\text{A.6})$$

where t is the current iteration, and the triangular2 mode reduces the amplitude by half each cycle.

Appendix B. Algorithms

Appendix B.1. Enhanced LoRA with Cyclical Scaling

Appendix B.2. GCViT Block with PEFT Window Attention

Algorithm 1 PEFT-GCViT Forward Pass

Require: Hyperspectral input $\mathbf{X} \in \mathbb{R}^{B \times C \times H \times W}$

Ensure: Class predictions $\mathbf{Y} \in \mathbb{R}^{B \times K}$

```
1: Phase 1: Spectral Feature Extraction
2:  $\mathbf{X}' \leftarrow \text{Unsqueeze}(\mathbf{X}, \text{dim} = 1)$  ▷  $\mathbb{R}^{B \times 1 \times C \times H \times W}$ 
3:  $\mathbf{X}' \leftarrow \text{Conv3D}_{7 \times 3 \times 3}(\mathbf{X}') \circ \text{BN3D} \circ \sigma_{\text{swish}}(\mathbf{X}')$  ▷ 1→32 channels
4:  $\mathbf{X}' \leftarrow \text{Conv3D}_{5 \times 3 \times 3}(\mathbf{X}') \circ \text{BN3D} \circ \sigma_{\text{swish}}(\mathbf{X}')$  ▷ 32→64 channels
5:  $\mathbf{X}' \leftarrow \text{Conv3D}_{3 \times 3 \times 3}(\mathbf{X}') \circ \text{BN3D} \circ \sigma_{\text{swish}}(\mathbf{X}')$  ▷ 64→dim channels
6:  $\mathbf{X}' \leftarrow \text{BandDropout}(\mathbf{X}', p = 0.1)$  ▷ Spectral regularization
7:  $\mathbf{F}_{\text{spec}} \leftarrow \text{SpectralAttention}(\mathbf{X}')$  ▷ Channel-wise attention
8:  $\mathbf{F}_{\text{spec}} \leftarrow \text{Mean}(\mathbf{F}_{\text{spec}}, \text{dim} = 2)$  ▷ Spectral dimension pooling
9: Phase 2: Patch Embedding & Positional Encoding
10:  $\mathbf{P} \leftarrow \text{PatchEmbed}(\mathbf{F}_{\text{spec}})$  ▷  $\mathbb{R}^{B \times \frac{H}{2} \times \frac{W}{2} \times d}$ 
11:  $\mathbf{P} \leftarrow \mathbf{P} + \mathbf{E}_{\text{pos}}$  ▷ Add learnable positional encoding
12:  $\mathbf{P} \leftarrow \text{Dropout}(\mathbf{P}, p = 0.1)$  ▷ Positional dropout
13: Phase 3: Hierarchical GCViT Processing
14: for  $\ell = 1$  to  $L$  do ▷  $L = 3$  hierarchical levels
15:   for  $b = 1$  to  $D_\ell$  do ▷  $D_\ell$  blocks per level  $\ell$ 
16:      $\mathbf{P} \leftarrow \text{GCViTBlock}_{\ell, b}(\mathbf{P})$ 
17:   end for
18:   if  $\ell < L$  then
19:      $\mathbf{P} \leftarrow \text{ReduceSize}_\ell(\mathbf{P})$  ▷ Spatial downsampling with SE
20:   end if
21: end for
22: Phase 4: Classification Head
23:  $\mathbf{F} \leftarrow \text{LayerNorm}(\text{Flatten}(\mathbf{P}))$ 
24:  $\mathbf{F} \leftarrow \text{GlobalAvgPool}(\mathbf{F})$  ▷ Global feature aggregation
25:  $\mathbf{Y} \leftarrow \text{LoRALinear}(\mathbf{F})$  ▷ LoRA-enhanced classifier
26: return  $\mathbf{Y}$ 
```

Algorithm 2 Cyclical LoRA-Enhanced Linear Transformation

Require: Input features $\mathbf{x} \in \mathbb{R}^d$, base weights $\mathbf{W} \in \mathbb{R}^{d_{\text{out}} \times d}$

Require: LoRA matrices $\mathbf{A} \in \mathbb{R}^{r \times d}$, $\mathbf{B} \in \mathbb{R}^{d_{\text{out}} \times r}$

Require: Scaling parameters α, r , cyclical factor γ_t

Require: Dropout rate p_{lorA}

Ensure: Enhanced output $\mathbf{y} \in \mathbb{R}^{d_{\text{out}}}$

- 1: $\mathbf{y}_{\text{base}} \leftarrow \mathbf{W}\mathbf{x}$ ▷ Base transformation
 - 2: $\mathbf{h} \leftarrow \text{Dropout}(\mathbf{A}\mathbf{x}, p = p_{\text{lorA}})$ ▷ LoRA down-projection with dropout
 - 3: $\mathbf{y}_{\text{lorA}} \leftarrow \mathbf{B}\mathbf{h}$ ▷ LoRA up-projection
 - 4: $s_t \leftarrow \frac{\alpha}{r} \cdot \gamma_t$ ▷ Cyclical scaling factor
 - 5: $\mathbf{y} \leftarrow \mathbf{y}_{\text{base}} + s_t \cdot \mathbf{y}_{\text{lorA}}$ ▷ Residual connection
 - 6: **return** \mathbf{y}
-

Algorithm 3 PEFT-GCViT Block Processing

Require: Input tokens $\mathbf{X} \in \mathbb{R}^{B \times H \times W \times d}$

Require: Window size M , number of heads h , LoRA rank r

Ensure: Output tokens $\mathbf{X}' \in \mathbb{R}^{B \times H \times W \times d}$

- 1: **Multi-Head Window Attention with LoRA:**
 - 2: $\mathbf{X}_{\text{norm}} \leftarrow \text{LayerNorm}(\mathbf{X})$
 - 3: $\mathbf{W} \leftarrow \text{WindowPartition}(\mathbf{X}_{\text{norm}}, M)$ ▷ $\mathbb{R}^{N_w \times M^2 \times d}$
 - 4: $\mathbf{QKV} \leftarrow \text{LoRALinear}(\mathbf{W})$ ▷ LoRA-enhanced QKV projection
 - 5: $\mathbf{Q}, \mathbf{K}, \mathbf{V} \leftarrow \text{Split}(\mathbf{QKV}, 3)$ ▷ Separate Q, K, V matrices
 - 6: **for** head $i = 1$ to h **do**
 - 7: $\mathbf{A}_i \leftarrow \text{Softmax}\left(\frac{\mathbf{Q}_i \mathbf{K}_i^T}{\sqrt{d_k}} + \mathbf{B}_{\text{rel}}\right)$
 - 8: $\mathbf{O}_i \leftarrow \mathbf{A}_i \mathbf{V}_i$
 - 9: **end for**
 - 10: $\mathbf{O} \leftarrow \text{Concat}(\mathbf{O}_1, \dots, \mathbf{O}_h)$
 - 11: $\mathbf{W}' \leftarrow \text{LoRALinear}(\mathbf{O})$ ▷ LoRA-enhanced output projection
 - 12: $\mathbf{X}_{\text{attn}} \leftarrow \text{WindowReverse}(\mathbf{W}', H, W)$
 - 13: $\mathbf{X}_{\text{res1}} \leftarrow \mathbf{X} + \text{DropPath}(\mathbf{X}_{\text{attn}})$
 - 14: **SwiGLU Feed-Forward Network:**
 - 15: $\mathbf{X}_{\text{norm2}} \leftarrow \text{LayerNorm}(\mathbf{X}_{\text{res1}})$
 - 16: $\mathbf{G}_1, \mathbf{G}_2 \leftarrow \text{Linear}_1(\mathbf{X}_{\text{norm2}}), \text{Linear}_2(\mathbf{X}_{\text{norm2}})$ ▷ Standard linear layers
 - 17: $\mathbf{H} \leftarrow \sigma_{\text{swish}}(\mathbf{G}_1) \odot \mathbf{G}_2$ ▷ SwiGLU gating mechanism
 - 18: $\mathbf{F} \leftarrow \text{Linear}_3(\mathbf{H})$ ▷ Final projection
 - 19: $\mathbf{X}' \leftarrow \mathbf{X}_{\text{res1}} + \text{DropPath}(\mathbf{F})$
 - 20: **return** \mathbf{X}'
-